Journal of the Taiwan Institute of Chemical Engineers 165 (2024) 105808

Contents lists available at ScienceDirect

Journal of the Taiwan Institute of Chemical Engineers

journal homepage: www.journals.elsevier.com/journal-of-the-taiwan-institute-of-chemical-engineers

Self-powered piezoelectric ultraviolet photodetectors based on TiO_2-NFs:P(VDF-TrFE) nanocomposites via ultraviolet-assisted thermal annealing for the prevention of ultraviolet overexposure

Jer-Chyi Wang [a,b,c,*], Tzu-Chuan Yang [a], Tzu-Wei Hsu [a], Ping-Jung Huang [a], Peng-Nang Chen [a], Chen-Yang Tseng [a], Ting-Han Lin [d], Jia-Mao Chang [d], Chang-Heng Liu [e], Wen-Ling Yeh [e,f,g,*], Ming-Chung Wu [d,h,i,*]

[a] Department of Electronic Engineering, Chang Gung University, Guishan Dist. 33302, Taoyuan, Taiwan
[b] Department of Neurosurgery, Chang Gung Memorial Hospital, Linkou Branch, Guishan Dist. 33305, Taoyuan, Taiwan
[c] Department of Electronic Engineering, Ming Chi University of Technology, Taishan Dist. 243303, New Taipei City, Taiwan
[d] Department of Chemical and Materials Engineering, Chang Gung University, Guishan Dist. 33302, Taoyuan, Taiwan
[e] Department of Orthopedic Surgery, Chang Gung Memorial Hospital, Linkou Branch, Guishan Dist. 33305, Taoyuan, Taiwan
[f] Department of Medicine, Chang Gung University, Guishan Dist. 33302, Taoyuan, Taiwan
[g] Department of Orthopedic Surgery, Chang Gung Memorial Hospital, Xiamen Branch, Haicang Dist. 361000, Xiamen, Fujian Province, China
[h] Division of Neonatology, Department of Pediatrics, Chang Gung Memorial Hospital, Linkou Branch, Guishan Dist. 33305, Taoyuan, Taiwan
[i] Center for Sustainability and Energy Technologies, Chang Gung University, Guishan Dist. 33302, Taoyuan, Taiwan

ARTICLE INFO

Keywords:
Ultraviolet index
Self-powered
Piezoelectric nanogenerators (PENGs)
Photodetectors
P(VDF-TrFE)
TiO_2-nanofibers

ABSTRACT

Background: Ultraviolet (UV) radiation overexposure due to severe ozone layer depletion increases the risk of skin cancer. However, the traditional UV index meter needs the power supply which is not convenient for outdoor use. The study aims to develop a UV overexposure warning system with a self-powered piezoelectric UV photodetector to provide a real-time UV index.
Method: A self-powered piezoelectric UV photodetector with TiO_2-nanofibers (TiO_2-NFs)-doped poly(vinylidene fluoride-trifluoroethylene) (P(VDF-TrFE)) nanocomposite films via ultraviolet-assisted thermal annealing was fabricated. A lumped circuit was designed to realize the stepping illumination of light-emitting diodes (LEDs) under continuous tapping of self-powered piezoelectric UV photodetectors.
Significant Findings: At a fixed 40-kPa pressure and 2-Hz frequency with varying UV irradiation power densities, the self-powered piezoelectric UV photodetectors exhibited outstanding UV detection capabilities, with a responsivity and detectivity for 0.14 mA/W and 4×10^8 Jones, respectively. A UV overexposure warning system was established by connecting a self-powered piezoelectric UV photodetector with a lumped circuit to achieve the stepping illumination of LEDs under continuous tapping, giving warnings for those performing outdoor activities to avoid UV overexposure.

1. Introduction

Given the continuous and excessive carbon dioxide and nitrous oxide emissions from fossil fuel combustion, ozone layer depletion has intensified [1], resulting in significant increases in the ultraviolet (UV) radiation intensity on Earth. Heightened UV exposure damages human skin, increasing the risks of sunburn and skin cancer [2–3]. Skin cancer affects over 2–3 million individuals yearly [4], underscoring the importance of detecting the UV exposure intensity when someone engages in outdoor activities to prevent UV overexposure. The World Health Organization (WHO) has provided 12 UV-exposure grades collectively known as the ultraviolet index (UVI) [5], which offers valuable information for humans to be aware of UV overexposure risks. UVI was established by the Commission Internationale de l'Eclairage according to the UV light erythematic spectrum on the human body and is primarily calculated by integrating the intensity across 250–400 nm wavelengths [6]. Researchers have investigated how skin type, UV dosage, and other factors affect the generation of skin sunburn by UV

* Corresponding authors:
E-mail addresses: jcwang@mail.cgu.edu.tw (J.-C. Wang), yeh610128@gmail.com (W.-L. Yeh), mingchungwu@cgu.edu.tw (M.-C. Wu).

https://doi.org/10.1016/j.jtice.2024.105808
Received 11 June 2024; Received in revised form 11 October 2024; Accepted 19 October 2024

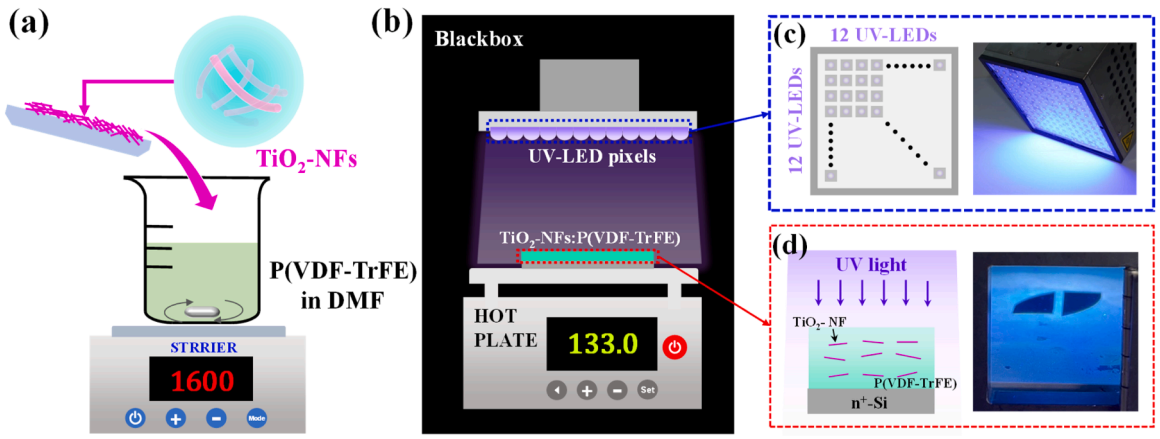

Fig. 1. (a) Schematic diagram of the TiO_2-NFs and P(VDF-TrFE) mixed procedure. The mixture was stirred at room temperature using a magnetic stirrer for at least 24 h (b) Schematic diagram of the new ultraviolet-assisted thermal annealing (UATA) system using a customized 12 × 12-pixel 365-nm UV light source at 133 °C. Schematic diagrams and photographs of (c) the UV-LED pixels and (d) UATA on TiO_2-NFs:P(VDF-TrFE) nanocomposite films.

radiation, to determine how UV exposure intensity and UVI levels correlate [7,8]. To acquire the UV exposure intensity, various semiconductor devices have been developed, such as metal-insulator-metal capacitors, field-effect transistors, heterojunction photodetectors, and nanogenerators (NGs) [9–12]. UV NGs are the most attractive because they eliminate the use of external power supplies for portable UV photodetectors, expanding their applications in bio-medicine, agriculture, military, and the environment [13]. UV-light-responsive materials are utilized in NGs to obtain photoelectric responses when exposed to UV light and generate electric power by applying external forces through piezoelectric or triboelectric effects [11,14]. Piezoelectric NGs (PENGs), which convert external stimuli into electricity via piezoelectricity [15], are the primary NGs for UV detection owing to their lightweight, cost-effectiveness, and high energy efficiency [16]. These advantages make PENGs promising candidates for portable and wearable UV detectors. Nevertheless, how the piezoelectric and photoelectric characteristics of PENGs relate under UV exposure remains unclear. Qin et al. proposed that the separation of photo-generated electron-hole pairs induced a built-in voltage, counteracting the reverse voltage of piezoelectric polarization for decreasing the output voltage [17]. In contrast, Zheng et al. suggested that the photo-generated electron-hole pairs excited by UV light interacted with polarization dipoles, enhancing piezoelectric polarization to increase the output voltage [18]. Consequently, UV-light-responsive piezoelectric materials with different light-absorption capabilities may contribute to different piezoelectric and photoelectric properties in PENGs.

The piezoelectric materials used in NGs are mainly inorganic ceramics and organic polymers. Compared to brittle perovskite ceramic materials, organic polymers such as polyvinylidene fluoride (PVDF) and its copolymer, poly(vinylidene fluoride-trifluoroethylene) (P(VDF-TrFE)), are desirable given their excellent flexibility, simple processing, and high stability [19,20]. P(VDF-TrFE) copolymers have four crystallization phases, namely α, β, γ, and δ phases [21]; the β-phase exhibits the best ferroelectric and piezoelectric properties owing to the well-aligned C-F bonds induced by TrFE in PVDF [22]. Fabricating processes such as annealing, electrospinning, and nanofiller doping enhance β-phase formation in P(VDF-TrFE) copolymers [21,23,24]. Incorporating methylammonium lead iodide nanoparticles with visible light absorption capability into piezoelectric thin films enhances power-generating properties and light-sensing capabilities in PENGs [25]. These nanofillers absorb visible light to generate electron-hole pairs, altering the polarization of piezoelectric materials and changing their characteristics to achieve visible light sensing.

For use in UV sensing, choosing nanofillers for doping into piezoelectric materials depends on their energy bandgaps. Options include metal-oxides, III-V semiconductors, and organic nanofillers with energy bandgaps of approximately 3.2 eV [26–29]. Metal-oxide nanofillers, which have the advantages of high stability, low cost, excellent electronic structure, and high UV-absorption properties, are widely implemented in UV sensing [30]. Among metal-oxide nanofillers, titanium dioxide nanofibers (TiO_2-NFs) are preferable given their excellent UV absorption capability, high photocatalytic activity, and strong chemical stability [31]. They exhibit 12 crystallization phases, where four distinct phases, rutile (tetragonal), anatase (tetragonal), brookite (orthorhombic), and monoclinic (β-TiO_2), are the most common and stable phases in natural environments, depending on the formation temperature [32]. Generally, when the formation temperature is below 500 °C, TiO_2-NFs are in the brookite phase, whereas they can be transformed into the anatase phase with a 3.04-eV energy bandgap at temperatures exceeding 500 °C [31,33]. Besides, the monoclinic phase (β-TiO_2) serves as the transition phase between brookite and anatase phases. If the processing temperature exceeds 800 °C, TiO_2-NFs with a rutile phase can form at a 3.2-eV energy bandgap [31,33]. Because of their high UV absorption capability, long carrier lifetime, and excellent carrier mobility, anatase-phase TiO_2-NFs exhibit superior photocatalytic properties for UV sensing compared to other phases of TiO_2-NFs [34]. Moreover, it was reported that some specific treatments on TiO_2-NFs would induce the transition phases, such as TiO_2-II, where the structures are analogous to baddeleyite (α-ZrO_2 structure) [35,36], cotunnite ($PbCl_2$ structure) [35,37], and srilankite (α-PbO_2) phases [35,38]. In this study, owing to the need of high UV absorption and photocatalytic activity, anatase-phase TiO_2-NFs were chosen and doped into P(VDF-TrFE) copolymers (TiO_2-NFs:P(VDF-TrFE)) and then annealed on a hot plate with 365-nm UV irradiation, which is called ultraviolet-assisted thermal annealing (UATA). During UATA treatment, UV photons were absorbed by TiO_2-NFs to generate electron-hole pairs, guiding dipole alignment in P(VDF-TrFE) films and enhancing polarization. Additionally, the TiO_2-NF doping concentration in the P(VDF-TrFE) copolymers and the UV light power density of UATA treatment were optimized by assessing the β-phase crystallinity and ferroelectric properties of the films. Subsequently, TiO_2-NFs:P(VDF-TrFE) PENGs were fabricated and measured in a dark space and UV irradiation environment to assess their UV detection characteristics and serve as UV photodetectors. To establish a UV overexposure warning system, a self-powered piezoelectric UV photodetector under continuous tapping and UV irradiation at different UVIs was connected to a lumped circuit to perform the stepping illumination of light-emitting diodes (LEDs), corresponding to the UVI levels. This UV detection technology can effectively warn individuals against UV overexposure during outdoor activities at high UVI levels.

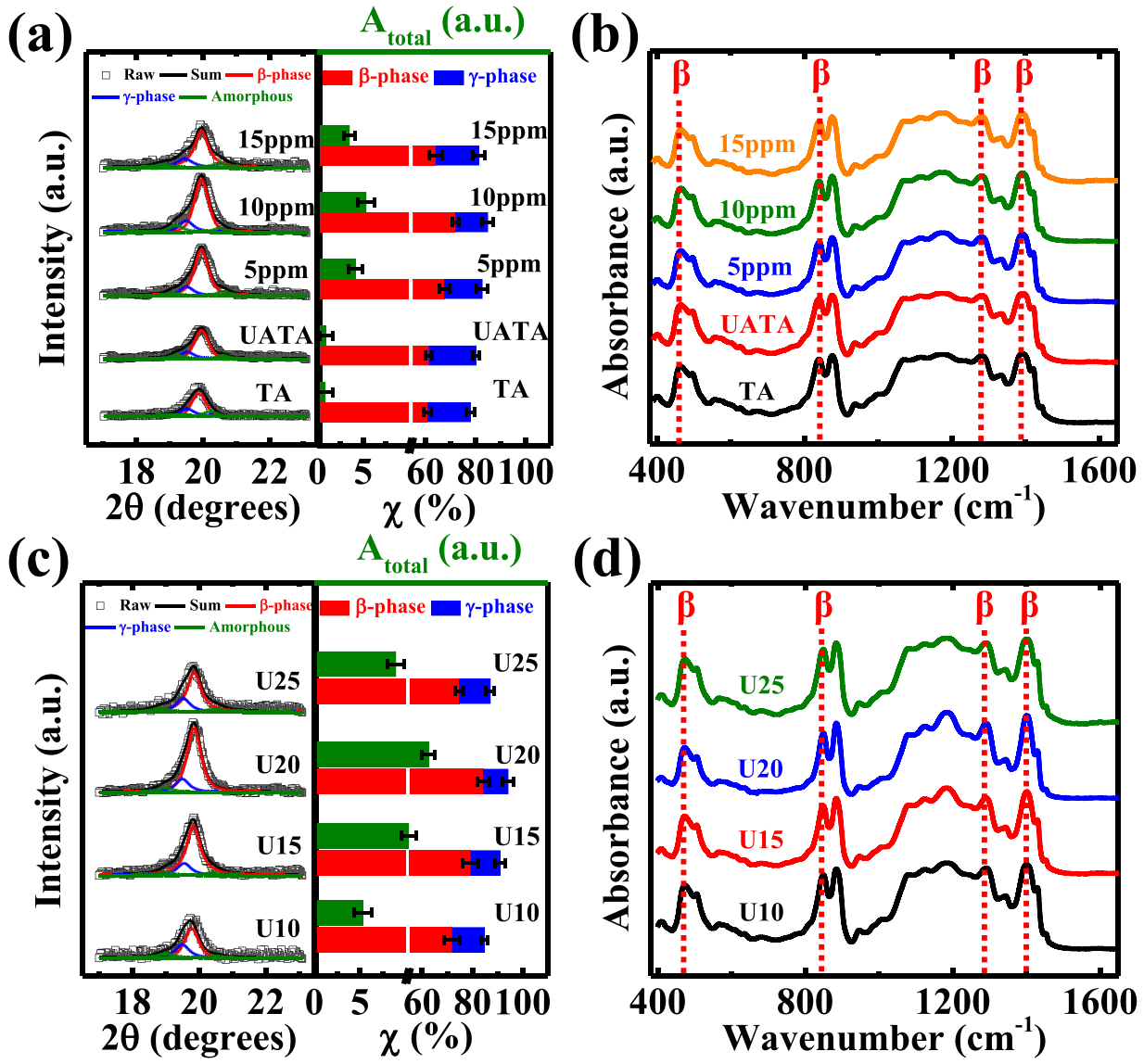

Fig. 2. (a) XRD patterns, the integrated area under the diffraction peaks, and the crystallization percentages of β- and γ-phases for the P(VDF-TrFE) films doped with different TiO_2-NF concentrations under UATA. (b) FTIR spectroscopy of the P(VDF-TrFE) films doped with different TiO_2-NF concentrations under UATA. (c) XRD patterns, the integrated area under the diffraction peaks, and the crystallization percentages of β- and γ-phases for the TiO_2-NFs:P(VDF-TrFE) nanocomposite films with a 10-ppm TiO_2-NF doping concentration under UATA at different UV power densities. (d) FTIR spectroscopy of the TiO_2-NFs:P(VDF-TrFE) nanocomposite films with a 10-ppm TiO_2-NF doping concentration under UATA at different UV power densities.

2. Experimental

2.1. Material synthesis

Anatase TiO_2-NFs were synthesized using a hydrothermal reaction with commercial anatase TiO_2 powder (Sigma-Aldrich, Burlington, Massachusetts, USA) as the source material. Initially, anatase TiO_2 powder was mixed in a 10-M sodium hydroxide (NaOH) solution. The mixture was transferred to a 1-L polytetrafluoroethylene-lined reactor and stirred for 30 min. Subsequently, the NaOH solution with anatase TiO_2 powder was heated to 160 °C for 24 h to conduct the hydrothermal reaction. After cooling to room temperature, the chemical reaction product was washed several times with deionized water until reaching a neutral pH of 7. Diluted hydrochloric acid was then added to the reactor for ion exchange, producing hydrogen titanate ($H_2Ti_3O_7$). To transform back to anatase TiO_2, $H_2Ti_3O_7$ was calcined at 600 °C for 12 h, yielding anatase TiO_2-NFs [39]. P(VDF-TrFE) (70/30 mol%) powder (Piezotech S.A.S., Arkema, Colombes, France) and dimethylformamide (DMF) solvent (Tedia Company, Inc., Fairfield, Ohio, USA) were used to prepare a TiO_2-NFs-doped P(VDF-TrFE) solution for ferroelectric film deposition. To acquire a homogeneous solution, P(VDF-TrFE) powder was first mixed in DMF at a fixed 5 wt% concentration and stirred with a magnetic stirrer until complete dissolution. After that, TiO_2-NFs were mixed with the P(VDF-TrFE) solution at different concentrations (0, 5, 10, and 15 ppm) and stirred at room temperature using a magnetic stirrer for at least 24 h (Fig. 1a).

2.2. Device fabrication

To fabricate metal-ferroelectric-metal (MFM) capacitors, n^+-Si wafers with resistivity of lower than 0.005 Ω·cm were used as substrates and treated as the bottom electrode (BE) of the devices. The wafers were cleaned using the standard Radio Corporation of America (RCA) procedure. To achieve a uniform TiO_2-NFs:P(VDF-TrFE) nanocomposite

film, a homogeneous solution was spin-coated onto the n^+-Si wafers at 750 rpm for 30 s with a 360-nm film thickness, measured using an ellipsometer (M-2000X, J.A. Woollam, USA). To perform crystallization of the TiO_2-NFs:P(VDF-TrFE) nanocomposite films, a new UATA system using a customized 12 × 12-pixel 365-nm UV light source at 133 °C was employed for 2 h, as illustrated in Fig. 1(b) and shown in the photograph of Fig. S1. Schematic diagrams and photographs of the UV-LED pixels and UATA process are shown in Fig. 1(c and d), respectively. To understand the influence of TiO_2-NFs during UATA, different TiO_2-NF doping concentrations in P(VDF-TrFE) films treated by the UATA at a UV light power density of 10-mW/cm^2 were investigated and labeled 5 ppm, 10 ppm, and 15 ppm (Table S1). The UV light power density was the average intensity of all UV-LEDs in this panel, which was confirmed by an optical power meter (843-R, Newport Corp., USA). For comparison, pure P(VDF-TrFE) films with conventional thermal annealing at 133 °C and UATA were fabricated and denoted as TA and UATA. After determining the optimal TiO_2-NF doping concentration in the P(VDF-TrFE) films, the UV light power densities of 10, 15, 20, and 25 mW/cm^2 were modified, and the fabricated devices were named U10, U15, U20, and U25 (Table S2). The U10 device (Table S2) corresponded to the 10 ppm device (Table S1). After that, a 300-nm-thick aluminum (Al) film was deposited on the samples using thermal evaporation with Al slugs (99.999 % purity). The top electrodes (TEs) were patterned using standard photolithography and wet-etched using an Al etching solution (H_3PO_4:HNO_3:CH_3COOH:H_2O=50:2:10:9) at 60 °C to form the TiO_2-NFs:P(VDF-TrFE) MFM capacitors.

To fabricate PENGs, n^+-Si wafers with specific heat capacity of approximately 0.7 J/kg·K at room temperature were cleaned using RCA and used as BEs [40], which can reduce the interference of pyroelectricity in the P(VDF-TrFE) films under prolonged exposure to sunlight. Subsequently, the TiO_2-NFs:P(VDF-TrFE) nanocomposite films were drop-casted onto the n^+-Si wafers and treated using UATA to enhance their β-phase crystallinity. Subsequently, transparent fluoride-doped tin oxide (FTO)-coated glass was pasted onto the samples and served as the TE, obtaining FTO/TiO_2-NFs:P(VDF-TrFE)/n^+-Si PENGs. Finally, copper foil tapes were used to contact the TEs and BEs and connected to a high-precision oscilloscope (RTE1024, Rohde & Schwarz, Germany).

2.3. Material characterization and device measurement

The crystalline structures of the TiO_2-NFs and TiO_2-NFs:P(VDF-TrFE) films were analyzed using X-ray diffraction (XRD) (D2 Phaser, Bruker, USA) at a fixed 5°/min scanning rate and both 10–80° and 17–23° scanning ranges. Meanwhile, the nanocomposite film crystallinity was examined via Fourier-transform infrared (FTIR) spectroscopy (Bruker Tensor 27 IR, Bruker, USA) at a 2-cm^{-1} resolution. Moreover, TiO_2-NF absorption spectrum was investigated via ultraviolet-visible (UV–Vis) spectrometry (V-730, JASCO, Japan). To observe the TiO_2-NF microstructure, the high-resolution transmission electron microscopy (HRTEM) (JEM-2100 Plus, JEOL, Japan) was employed at a 200-kV acceleration voltage. Subsequently, field-emission scanning electron microscopy (FE-SEM) (SU8010, Hitachi, Japan) at a 5-kV acceleration voltage and 8 × 10^4 magnification was utilized to investigate the surface morphology of the TiO_2-NFs:P(VDF-TrFE) nanocomposite films.

For electrical characterization of the TiO_2-NFs:P(VDF-TrFE) MFM capacitors, the polarization versus electric field ($P-E$) hysteresis loops, current density versus electric field ($J-E$) curves, and frequency-dependent dielectric properties were analyzed using a semiconductor analyzer (Keithley 4200-SCS, Tektronix, Inc., USA). Additionally, the piezoelectric coefficients (d_{33}) were recorded using a d_{33} meter (YE2730, Sinoceramics, Inc., China). To obtain the output characteristics of the TiO_2-NFs:P(VDF-TrFE) PENGs, periodic pressure was applied using a handmade shaker, and the open-circuit voltage (V_{oc}) and short-circuit current (I_{sc}) were recorded using a high-precision oscilloscope (RTE1024, Rohde & Schwarz, Inc., USA). To measure the V_{oc}, the PENG was connected to the oscilloscope in parallel. On the other hand, to measure the I_{sc}, a multi-channel power probe (RT-ZVC02, Rohde & Schwarz, Inc., USA) was applied and connected to the PENG in series.

3. Results and discussion

3.1. Material properties of *TiO$_2$-NFs:P(VDF-TrFE)* nanocomposites with UATA

For UATA, the microstructure and crystalline structure of TiO_2-NFs were vital for the efficient absorption of UV light [39]. After the hydrothermal reaction, the TiO_2 powder was successfully transformed into perfect TiO_2-NFs with diameters of ~40 nm, as shown in the HRTEM image of Fig. S2(a). Fig. S2(b) presents the crystalline TiO_2-NF structure analyzed by XRD with the characteristic peaks of 2θ at 25.5°, 38.0°, 48.3°, 54.1°, 55.3°, 62.9°, and 68.9°, representing the crystallinity of (101), (200), (211), (204), (116), (220), and (215), respectively. According to JCPDS card no. 21–1272, all seven peaks correspond to the anatase phase of TiO_2 [39]. Fig. S2(c) displays the UV–Vis absorption spectrum of TiO_2-NFs, showing the highest absorption at a wavelength of 360 nm. The results confirm that the fabricated anatase TiO_2-NFs exhibited strong UV absorption capability and photocatalytic properties. These characteristics made them suitable nanofillers, maximizing the UATA crystallization efficiency in P(VDF-TrFE) films and providing excellent generation of electron-hole pairs under UV light exposure during PENG measurement.

Fig. 2(a) shows XRD patterns, the integrated area under the diffraction peaks, and the crystallization percentages of β- and γ-phases for the P(VDF-TrFE) films doped with different TiO_2-NF concentrations under UATA. In the left of Fig. 2(a), a distinct diffraction peak at approximately 2θ = 20° occurs, representing the electroactive phase of P(VDF-TrFE) copolymers. Additionally, the intensity of the diffraction peaks increased with increasing TiO_2-NF doping concentration and was optimized at 10 ppm. For the P(VDF-TrFE) films doped with a TiO_2-NF concentration of 15 ppm, the diffraction peak decreased slightly, indicating that too many TiO_2-NFs degraded the P(VDF-TrFE) film crystallinity, as discussed later. To precisely quantize the electroactive phases in TiO_2-NFs:P(VDF-TrFE) nanocomposite films, the area under the diffraction peaks at 2θ = 20.1° and 20.5° were integrated, corresponding to the γ(002) and β(200)/(110) phases of P(VDF-TrFE) copolymers, respectively [41,42]. Thus, their crystallization percentages were calculated as follows [43]:

$$\chi_\beta = \frac{A_\beta}{A_{\text{total}}} \times 100\% \quad (1)$$

$$\chi_\gamma = \frac{A_\gamma}{A_{\text{total}}} \times 100\% \quad (2)$$

$$A_{\text{total}} = A_\beta + A_\gamma + A_{\text{am}} \quad (3)$$

where A_β, A_γ, and A_{am} represent the areas under the diffraction peaks of β-, γ-phases, and the amorphous type, respectively; A_{total} is the total area under diffraction peaks. The crystallization percentages of β- and γ-phases and the total area under diffraction peaks were calculated to plot the statistical distributions, as presented in the right of Fig. 2(a). For the pure P(VDF-TrFE) films under the TA and UATA treatments, the crystallization percentages of β- and γ-phases remained consistent for approximately 61 % and 17 %, respectively, owing to the non-absorptiveness of UV light in P(VDF-TrFE) copolymers [44,45]. With the doping of 10-ppm TiO_2-NFs in P(VDF-TrFE) films, the crystallization percentage of the β-phase increased significantly to 71.9 %, which could be used to optimize UATA to boost electroactive and photocatalytic behaviors.

To further confirm the crystallinity of TiO_2-NFs:P(VDF-TrFE) nanocomposite films, FTIR spectroscopy was examined, as shown in Fig. 2(b). The characteristic peaks of the electroactive phases in the P(VDF-TrFE) copolymers at wavenumbers of 475, 840, 1288, and 1400 cm^{-1} were

Table 1
Calculated proportions of β- and γ-phase crystallinity for the P(VDF-TrFE) film under TA and the P(VDF-TrFE) films doped with different TiO_2-NF concentrations under UATA.

Sample	TA	UATA	5ppm	10ppm	15ppm
F_{EA}	71.6 %	71.8 %	73.3 %	78.2 %	72.2 %
F_{β}	56.6 %	57.0 %	60.7 %	64.9 %	58.4 %
F_{γ}	15.0 %	14.8 %	13.6 %	13.3 %	13.8 %

Table 2
Calculated proportions of β- and γ-phase crystallinity for the TiO_2-NFs:P(VDF-TrFE) nanocomposite films with a 10-ppm TiO_2-NF doping concentration under UATA at different UV power densities.

Sample	U10	U15	U20	U25
F_{EA}	78.2 %	83.5 %	85.2 %	81.5 %
F_{β}	64.9 %	70.5 %	73.2 %	68.3 %
F_{γ}	13.3 %	13.0 %	12.0 %	13.2 %

only slightly enhanced by TiO_2-NF doping. For more detailed analyses of the electroactive phases, the crystallinity was calculated using the Beer-Lambert law [46,47]:

$$F_{EA} = \frac{A_{EA}}{(K_{EA}/K_{NEA}) \times A_{NEA} + A_{EA}} \times 100\% \quad (4)$$

where F_{EA} represents the crystallinity of the electroactive phase; A_{EA} and A_{NEA} are the absorbance of the electroactive and non-electroactive phases, located at wavenumbers of 840 and 880 cm^{-1}, respectively. Besides, K_{EA} and K_{NEA} are the absorption coefficients at 840 and 880 cm^{-1} for 6.1 × 10^{-4} and 7.7 × 10^{-4} cm^2/mol, respectively [48]. The calculated F_{EA} values are listed in Table 1. With TiO_2-NF doping into the P(VDF-TrFE) films, the crystallinity of the electroactive phase increased from 71.2 % to 78.2 %, exhibiting similar trends to the XRD results (Fig. 2a). Since β and γ crystalline phases belonged to the electroactive phase of P(VDF-TrFE) copolymers, the proportions of polar β- and semipolar γ-phase crystallinity were calculated as follows [49,50]:

$$F_{\beta} = F_{EA} \times \left(\frac{\Delta A_{\beta}}{\Delta A_{\beta} + \Delta A_{\gamma}}\right) \times 100\% \quad (5)$$

$$F_{\gamma} = F_{EA} \times \left(\frac{\Delta A_{\gamma}}{\Delta A_{\beta} + \Delta A_{\gamma}}\right) \times 100\% \quad (6)$$

where F_{β} and F_{γ} are the proportions of β- and γ-phase crystallinity, respectively; ΔA_{β} represents the difference in absorbance between the characteristic peak at 1275 cm^{-1} and the nearest valley around 1260 cm^{-1}; ΔA_{γ} represents the difference in absorbance between the characteristic peak at 1234 cm^{-1} and the nearest valley around 1225 cm^{-1}. The calculated proportions of β- and γ-phase crystallinity are listed in Table 1. When the TiO_2-NF doping concentration increased to 10 ppm, the proportion of the β-phase crystallinity in the TiO_2-NFs:P(VDF-TrFE) nanocomposite films increased by approximately 8.3 %, while that of the γ-phase decreased by 1.7 %, compared to the pure P(VDF-TrFE) films under the TA and UATA treatments. This trend was attributed to interactions between the TiO_2-NFs and the arranged dipoles for the phase transformation from the γ- to the β-phase. However, excessive TiO_2-NF doping in the P(VDF-TrFE) copolymers to 15 ppm could disrupt the dipole arrangement, decreasing crystallinity.

Fig. 2(c) shows the XRD patterns, the integrated area under the diffraction peaks, and the crystallization percentages of β- and γ-phases for the TiO_2-NFs:P(VDF-TrFE) nanocomposite films with a 10-ppm TiO_2-NF doping concentration under UATA at different UV power densities. According to Eqs. (1) to (3), the integrated area under the diffraction peaks and the crystallization percentages of the β- and γ-phases of the TiO_2-NFs:P(VDF-TrFE) nanocomposite films were calculated, as depicted in the right of Fig. 2(c). With increasing UV power density during UATA, the crystallization percentage of the β-phase increased significantly, reaching a maximum of approximately 84.3 % in the U20 sample. When the UV power density exceeded 25 mW/cm^2, the crystallization percentage of the β-phase decreased by approximately 10 % compared to that with a 20-mW/cm^2 UV power density. Fig. 2(d) shows the FTIR spectra of the nanocomposite films with UATA at different UV power densities. Similarly, the crystallinity of the electroactive phase and proportions of the polar β- and semipolar γ-phases were analyzed using the Beer-Lambert law, as formulated in Eqs. (4) to (6) (Table 2). For the samples with UATA at 20-mW/cm^2 UV power density, the crystallinity of the electroactive phase and proportions of the polar β-phase crystallinity increased to over 85.2 % and 73.2 %, respectively. This was attributed to more UV light being absorbed by TiO_2-NFs to generate more photon-induced electron-hole pairs in the nanocomposite films through the photocatalytic reaction, aligning the γ-phase into the β-phase dipoles. Nevertheless, if the UV power density exceeded 25 mW/cm^2, excessive generation of electron-hole pairs and too much UV radiation during UATA disturbed the alignment of polarized dipoles in the P(VDF-TrFE) films and degraded the P(VDF-TrFE) polymer matrix [51], respectively, decreasing the polar β-phase crystallinity. In Fig. 2, both XRD patterns and FTIR spectra corroborated that the TiO_2-NFs:P(VDF-TrFE) nanocomposite films with UATA at a moderate 20-mW/cm^2 UV light power density generated sufficient photon-induced electron--hole pairs through the photocatalytic reaction by TiO_2-NFs, facilitating optimal alignment of polarized dipoles in P(VDF-TrFE) films for further applications in self-powered piezoelectric UV photodetectors.

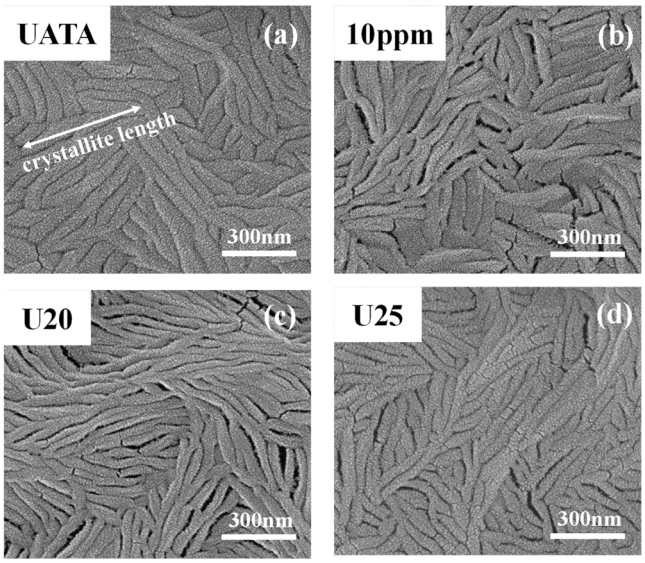

Fig. 3. Surface morphology images of the P(VDF-TrFE) films (a) without and with a 10-ppm TiO_2-NF doping concentration under UATA at (b) 10, (c) 20, and (d) 25 mW/cm^2. The crystallite length used to quantify the crystalline characteristics of these samples was marked in arrow in (a).

Fig. 3(a and b), and S3(a)-(c) show surface morphology images of the P(VDF-TrFE) films doped with different TiO_2-NF concentrations under TA and UATA treatments. All samples exhibited needle-like β-phase crystallinities, indicating significant electroactive crystallization for TiO_2-NFs:P(VDF-TrFE) nanocomposite films with TA and UATA treatments. To quantify the crystalline characteristics, the crystallite length, density, and filling factor in these images were analyzed. The crystallite length was denoted by the arrow in Fig. 3(a) [52], and the crystallite density and filling factor were defined by the amount and percentage of needle-shaped crystalline in the SEM images [53]. Statistical distributions of the crystallite length, density, and filling factor are plotted in Fig. S3(d)-(f), respectively. There was approximately no change in crystallite length, density, and filling factor of the P(VDF-TrFE) films

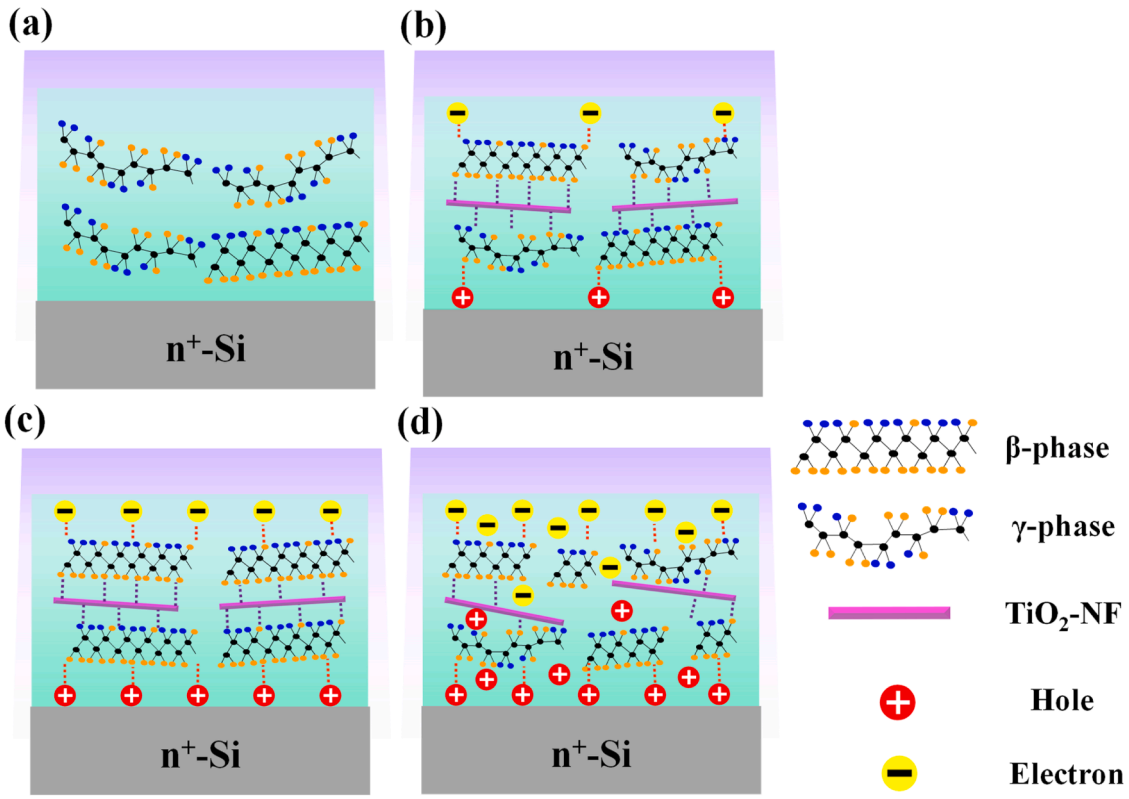

Fig. 4. Schematic diagrams to illustrate the change in the electroactive phases of the P(VDF-TrFE) films (a) without and with a 10-ppm TiO_2-NF doping concentration under UATA at (b) 10, (c) 20, and (d) 25 mW/cm^2.

with TA and UATA treatments, consistent with the fact that UV light cannot be absorbed by the P(VDF-TrFE) films. For P(VDF-TrFE) films doped with 10-ppm TiO_2-NFs under UATA, the crystallite length, density, and filling factor increased significantly, indicating a more pronounced generation of the β-phase crystallinity in this sample compared to that in the UATA sample, corresponding to the XRD and FTIR trends in Fig. 2. Fig. 3(c and d), and S4(a),(b) show surface topography images of the TiO_2-NFs:P(VDF-TrFE) nanocomposite films with a 10-ppm TiO_2-NF doping concentration under UATA at different UV power densities. Similarly, the crystallite length, density, and filling factor of these samples were analyzed to plot their statistical distributions, as shown in Fig. S4(c)-(e), respectively. The crystallite length of the U20 sample increased considerably from 416 to 819 nm, accompanied by a denser crystalline structure, compared with that of the U10 sample. The increased UV light power density during UATA effectively increased the generation of β-phase crystallinity in the nanocomposite films. However, a slight decrease in crystallite length, density, and filling factor was observed in the U25 sample, meaning that too much UV light irradiation deteriorated the arrangement of β-phase crystallinity in the TiO_2-NFs:P(VDF-TrFE) nanocomposite films.

3.2. *Output characteristics of piezoelectric nanogenerators with UATA-treated* ***TiO_2-NFs:P(VDF-TrFE)*** *nanocomposite films*

Based on the previous-discussed material analyses, a mechanism for the change in the electroactive phases of the TiO_2-NFs:P(VDF-TrFE) nanocomposite films upon UATA was established. Owing to the non-absorptiveness of UV light in P(VDF-TrFE) copolymers, only thermal annealing induces crystallization, resulting in a less electroactive phase as illustrated in Fig. 4(a). With appropriate TiO_2-NF doping in the P(VDF-TrFE) films with UATA, the TiO_2-NFs absorbed UV light to generate electron-hole pairs through a photocatalytic effect, thereby assisting the P(VDF-TrFE) copolymers in aligning dipoles to promote the generation of β-phase crystallinity (Fig. 4b), as revealed by the XRD and FTIR spectra of Fig. 2(a and b). Thus, an increase in polarization was obtained in the ferroelectric hysteresis, as shown in Fig. S5(a), contributing to the enhanced permittivity for the samples with a TiO_2-NF doping concentration of 10 ppm (Fig. S5(c)) [46]. Fortunately, only a slight increase in leakage current and dielectric loss of the P(VDF-TrFE) films with the doping of TiO_2-NFs was observed, as shown in Fig. S5(b) and (c). In Fig. 4(c), with increasing UV light power density of the UATA, more electron-hole pairs were generated to align the dipoles more directionally in the P(VDF-TrFE) films, leading to the generation of more β-phase crystallinity for an enhanced polarization. However, if the UV light power density of the UATA was too strong (Fig. 4d), excessive electron-hole pairs would disturb the dipole alignment, and excessive UV radiation would damage the P(VDF-TrFE) copolymers for the degraded polarization and unwanted leakage paths, as confirmed by the ferroelectric hysteresis and dielectric properties in Fig. S5(d)-(f); these results are described in Supporting Note S1.

Then, the piezoelectric properties of the TiO_2-NFs:P(VDF-TrFE) nanocomposite films with UATA were analyzed, as shown in Fig. 5. First, the piezoelectric coefficient (d_{33}) was examined to present a decreasing trend with an increase in the applied force from 1 to 2 N at an oscillation frequency of 110 kHz (Fig. 5a). When the force applied to the piezoelectric TiO_2-NFs:P(VDF-TrFE) nanocomposite films increased, the deformation space for the film compression continuously decreased, giving rise to a decrease in piezoelectric polarization [53]. When the UV light power density of the UATA was increased from 10 to 20 mW/cm^2, the d_{33} of the TiO_2-NFs:P(VDF-TrFE) nanocomposite films increased significantly from 40 to 55 pC/N, which was larger than that of the pure P(VDF-TrFE) film by approximately 23 pC/N [54]. Nevertheless, a further increase in UV light power density induced a noticeable degradation in d_{33}, which is consistent with the trend observed in the material analyses and ferroelectric properties discussed above. Meanwhile, the TiO_2-NFs:P(VDF-TrFE) PENGs with UATA at different UV light power

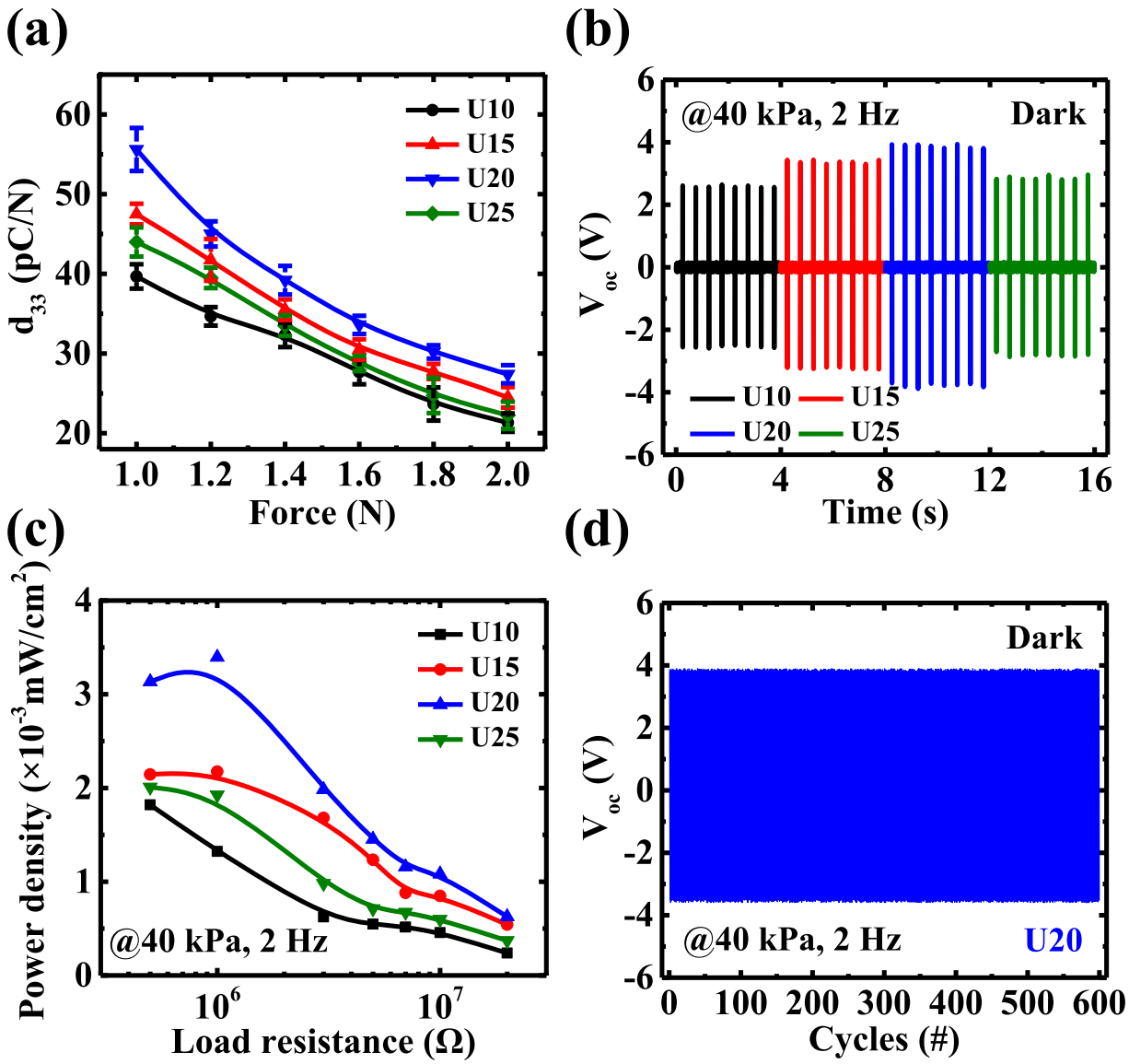

Fig. 5. (a) Piezoelectric coefficient (d_{33}) versus force characteristics of the TiO_2-NFs:P(VDF-TrFE) nanocomposite films with a 10-ppm TiO_2-NF doping concentration under UATA at different UV power densities. The force from 1 to 2 N was applied at an oscillation frequency of 110 kHz. (b) V_{oc} waveforms of the TiO_2-NFs:P(VDF-TrFE) PENGs under the application of a 40-kPa pressure at a 2-Hz frequency in a dark environment. (c) Power density versus load resistance characteristics of the TiO_2-NFs:P(VDF-TrFE) PENGs. (d) Cycling endurance tests of the U20 PENG in a dark environment. Even after 600 cycles, no degradation of the V_{oc} waveform was observed.

densities were fabricated, and their V_{oc} and I_{sc} were measured in a darkroom to evaluate their self-powered capabilities. Fig. 5(b) shows the V_{oc} waveforms of the TiO_2-NFs:P(VDF-TrFE) PENGs under the application of a 40-kPa pressure at a 2-Hz frequency. Additionally, the V_{oc} and I_{sc} waveforms of the devices were measured under different applied pressures at a 2-Hz frequency, as shown in Figs. S6 and S7, respectively. Under the application of a 40-kPa pressure, the maximum V_{oc} and I_{sc} values of the U20 PENG were 3.88 V and 4.55 μA, respectively. Compared with U10, the U20 PENG exhibited approximately 150 % and 207 % improvements in V_{oc} and I_{sc}, respectively. To analyze the output performance for energy harvesting, different load resistances were series to TiO_2-NFs:P(VDF-TrFE) PENGs and the voltage across the load resistor was measured under the application of a 40-kPa pressure at a 2-Hz frequency, as shown in the waveforms of the voltage across the load resistor (Fig. S8). Subsequently, the power density was calculated by using the formula: $P = V_L^2/(R_L \times S)$, where V_L and R_L are the voltage and resistance of the load resistor, respectively, and S is the force area of the PENGs. Fig. 5(c) shows the power density versus load resistance characteristics of the TiO_2-NFs:P(VDF-TrFE) PENGs. The U20 PENG presented the highest power density, 3.5×10^{-3} mW/cm^2, at a 1-MΩ load resistor, demonstrating excellent output characteristics. To confirm the repeatability of the U20 PENG, cycling endurance tests were performed, as shown in Fig. 5(d). Even after 600 cycles, no degradation of the V_{oc} waveform was observed, indicating the robustness of the TiO_2-NFs:P(VDF-TrFE) PENGs for UV light detection.

To investigate the photo-detection characteristics of the PENGs, a fixed pressure of 40 kPa was applied at a 2-Hz frequency with UV light irradiation at different power densities. The I_{sc} values of these devices were recorded using an oscillator, and the measurement results are shown in Fig. 6(a and b), and S9(a),(b). Statistical analysis of the I_{sc} of all samples under UV light irradiation at different power densities is presented in Fig. S9(c). When the power density of the UV light increased, a significant increase in I_{sc} was observed for all samples. Notably, the U20 sample exhibited the highest responsive current of more than 15 μA, which was consistent with the trend obtained in the piezoelectric output characteristics in Fig. 5. To further quantify the photo-detection

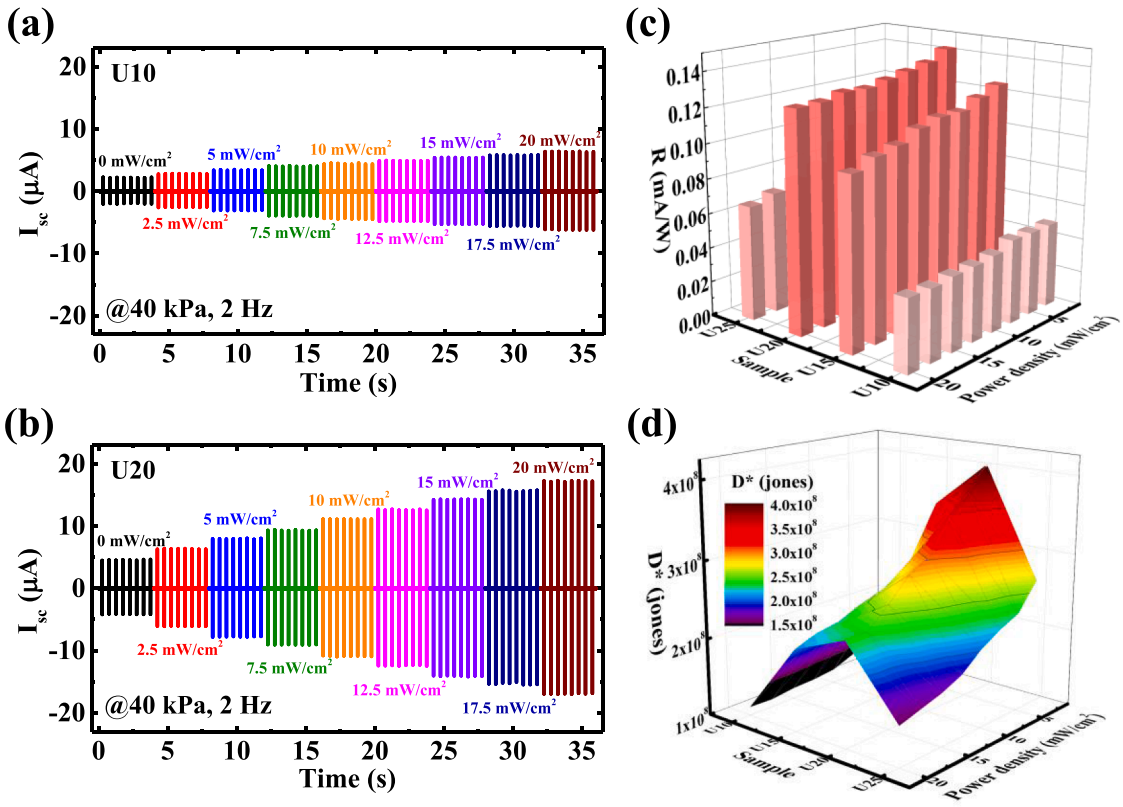

Fig. 6. Photo-detection characteristics of the (a) U10 and (b) U20 PENGs. A fixed pressure of 40 kPa was applied at a 2-Hz frequency with UV light irradiation at different power densities. Statistical analyses of (c) responsivity and (d) detectivity of the PENGs under UV light irradiation at different power densities.

characteristics of the UATA-treated TiO_2-NFs:P(VDF-TrFE) PENGs at different UV light power densities, which served as self-powered piezoelectric UV photodetectors, the responsivity (R), detectivity (D^*), and external quantum efficiency (EQE) were calculated using the following equations [55–58]:

$$R = (I - I_0)/(P_{UV} \times S) \tag{7}$$

$$D^* = R \times (S/2eI_0)^{0.5} \tag{8}$$

$$EQE = (R \times hc / e\lambda) \times 100\% \tag{9}$$

where I_0 and I represent the I_{sc} in the dark and UV light environments, respectively. Besides, P_{UV}, S, e, h, c, and λ are the UV light intensity, UV light irradiation area, electron charge, Planck constant, light speed, and wavelength, respectively. Statistical analyses of responsivity, detectivity, and EQE of all samples under UV light irradiation at different power densities are shown in Fig. 6(c and d), and S9(d), respectively. Notably, the U20 sample demonstrated excellent photo-detection characteristics in terms of responsivity, detectivity, and EQE, reaching 0.14 mA/W, 4×10^8 jones, and 4.5 %, respectively. The superior photo-detection behavior could be attributed to the electron-hole pairs generated by the UV light via TiO_2-NFs, which assisted in the alignment of piezoelectric dipoles in the P(VDF-TrFE) copolymers under the application of pressure, thus significantly enhancing the piezoelectric I_{sc}. Thus, the pressure-dependent photo-detection characteristics of this sample were investigated, as shown in the output waveforms of Fig. 6(b) and S10, respectively. Statistical analyses of the I_{sc}, responsivity, detectivity, and EQE of the U20 sample under UV light irradiation at different pressures are presented in Fig. S11. With an increase in applied pressure, the I_{sc} of the U20 sample was gradually increased, meaning that a higher pressure could enhance the piezoelectric characteristics of PENGs. On the other hand, the responsivity, detectivity, and EQE of the sample were almost the same under the application of different pressures, which implied that the applied pressure was independent of the photo-detection characteristics of our self-powered piezoelectric UV photodetectors. Finally, the photo-detection characteristics of our UATA-treated TiO_2-NFs:P

Table 3
Photo-detection characteristics of our UATA-treated TiO_2-NFs:P(VDF-TrFE) and previously proposed PVDF-related self-powered piezoelectric photodetectors.

Structures	Light source	V_{oc} (V) (Dark)	I_{sc} (μA) (Dark)	V_{oc} (V) (Light)	I_{sc} (μA) (Light)	R (mA/W)	D* (Jones)	EQE (%)	Refs.
ITO/ZnO:PVDF/Al	UV	17.5	–	15	–	–	–	–	[17]
ITO/MAPI:PVDF/ITO	Visible	2	0.03	0.75	0.08	–	–	–	[25]
ITO/$C_3H_7NH_3PbI_3$:PVDF/ITO	Visible	4.5	1	–	7	2.0×10^{-5}	3.7×10^7	4.6×10^{-3}	[59]
Ag/GO:PVDF/Ag	Visble	–	2.2	–	6.2	2.6×10^{-5}	3.1×10^7	6.2×10^{-3}	[60]
ITO/C_3N_4:PVDF/Al	Visble	2.5	0.04	0.02	–	1.7×10^{-3}	–	–	[61]
FTO/TiO_2-NFs:P(VDF-TrFE) /n^+-Si	**UV**	**4**	**4.5**	**10**	**15**	**0.14**	**4.0×10^8**	**4.5**	**This work**

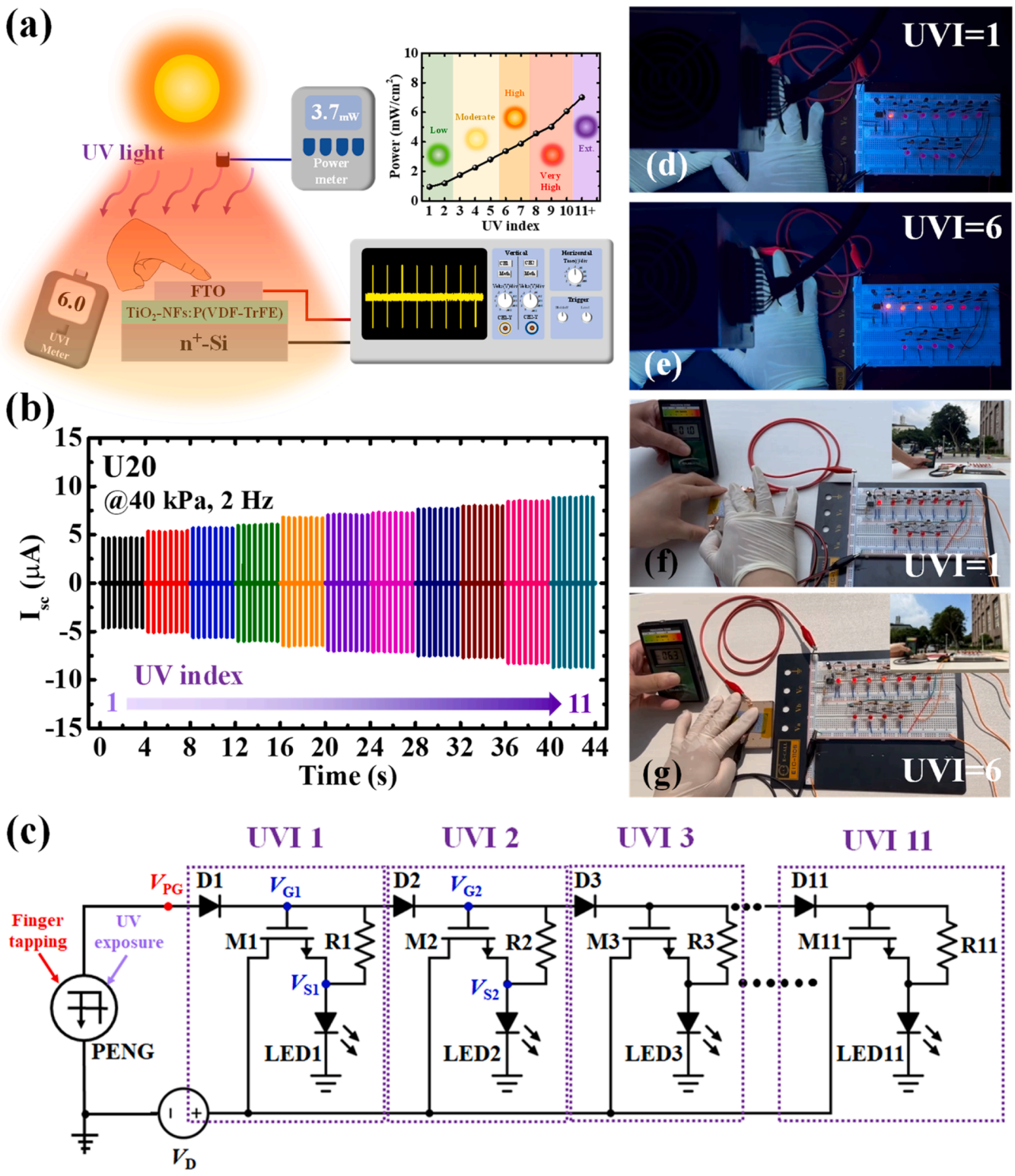

Fig. 7. (a) Schematic diagram of the measurement setup for UVI detection via the TiO_2-NFs:P(VDF-TrFE) self-powered piezoelectric UV photodetectors. The inset shows the relationship between UV light power densities and UVI levels analyzed using an optical power meter and a UVI meter. (b) I_{sc} waveforms of the U20 self-powered piezoelectric UV photodetectors under irradiation at different UVI levels were investigated using an oscilloscope. (c) Circuit diagram to light up a corresponding number of LEDs when the self-powered piezoelectric UV photodetector was irradiated to different intensities of UV light (UVI 1 ~ 11) under a continuous finger tapping. Photographs of the self-powered piezoelectric UV photodetector under continuous tapping to light up (d) one and (e) six LEDs under the irradiation of UV light with a UVI of 1 and 6, respectively. Photographs of the self-powered piezoelectric UV photodetector under continuous tapping to light up (f) one LED in cloudy weather with a UVI of 1 and (g) six LEDs in sunny weather with a UVI of 6. The measurements were performed outdoors at the same location under different weather conditions.

(VDF-TrFE) and previously proposed PVDF-related self-powered piezoelectric photodetectors are summarized in Table 3. Comparing to those of previous studies [17,25,59–61], our optimized devices presented the best output current of approximately 4.5 and 15 μA in dark and UV light environments, respectively. The superior photo-detection characteristics obtained in this study demonstrate a significant advancement in the development of self-powered piezoelectric UV photodetectors by utilizing UATA in TiO_2-NFs:P(VDF-TrFE) nanocomposite films.

3.3. *Self-powered piezoelectric UV photodetectors with UATA-treated* ***TiO_2-NFs:P(VDF-TrFE)*** *nanocomposite films for UV index detection*

In practical applications, the TiO_2-NFs:P(VDF-TrFE) self-powered piezoelectric UV photodetectors were implemented for UVI detection. This novel photodetector serves as a warning system for individuals engaged in outdoor activities, preventing overexposure to UV radiation and potential sunburn. A schematic diagram of the measurement setup is illustrated in Fig. 7(a). To validate the output characteristics of the self-powered piezoelectric UV photodetectors under UV irradiation, UV light from sunlight was simulated using a custom-made UV light source and the measurements were conducted in a blackbox. Initially, the relationship between UV light power densities and UVI levels was analyzed using an optical power meter (843-R, Newport Corporation, USA) and a UVI meter (Model 6.5R, Solarmeter, USA), respectively, as shown in the top-right inset of Fig. 7(a). The V_{oc} and I_{sc} waveforms of the self-powered piezoelectric UV photodetectors under irradiation at different UVI levels were investigated using an oscilloscope, as shown in Fig. 7(b) and S12 (a), respectively. Consequently, the UVI values could be acquired according to the V_{oc} and I_{sc} versus UVI characteristics, as presented in Fig. S12(b) and (c), respectively. The measurement not only correlated the output characteristics of the self-powered piezoelectric UV photodetectors with the UVI values but also provided relevant information for the circuit design of the stepping illumination of LEDs.

A circuit that enables the self-powered piezoelectric UV photodetector to light up a corresponding number of LEDs when irradiated with different intensities of UV light under continuous tapping was designed, as shown in the circuit diagram and lumped circuit on a breadboard of Fig. 7(c) and S13, respectively, with the details of relevant components listed in Table S3. For the circuit design principles to perform the stepping illumination of LEDs, 11 individual sections representing UVI 1 to 11 were divided with identical components. Taking the sub-circuit of UVI 1 for example, the diode (D1) primarily acted as a switch to determine whether the voltage signal could pass through or not. Additionally, it could rectify the output voltage (V_{PG}) provided by the TiO_2-NFs:P(VDF-TrFE) self-powered piezoelectric photodetectors under the application of a fixed pressure and the illumination of UV light at different UVI values. If the V_{PG} exceeded the cut-in voltage of the diode for approximately 0.5 V, the voltage signal of V_{PG} − 0.5 V, i.e. V_{G1}, was applied to the gate of the MOSFET (M1), otherwise the subsequent circuitry would be interrupted. The MOSFETs in this circuit served as switches to drive the LEDs. The drain voltage (V_D) of the MOSFETs for 1 V was supplied via a power supply and a resistor (R1) across the gate and source of M1 was applied to modulate the V_{GS} of the device. Initially, the source voltage of M1 (V_{S1}) was quite small because the effective resistance of LEDs was extremely small, which was insufficient to turn the LED1 on. When the V_{GS} exceeded the threshold voltage (V_t) of M1 for approximately 0.7 V, the device turned on, allowing the V_{S1} to be approximately equal to 1 V, thereby the LED1 illuminated. The resistance value of the resistors (R1 to R11) was adjusted to 5.1 kΩ to match the output voltage generated by the TiO_2-NFs:P(VDF-TrFE) self-powered piezoelectric photodetectors under the application of a fixed pressure of 40 kPa and the illumination of UV light at different UVI values, as shown in Fig. S12(a). Fig. S14(a) demonstrates the characteristics of the LED illumination under continuous tapping of the self-powered piezoelectric UV photodetector in a darkroom, which was screenshot from Video S1. If there was no UV light irradiation on the self-powered piezoelectric UV photodetector, the LEDs remained unlit due to the insufficient output voltage to activate the LEDs. Under the irradiation of UV light with a UVI of 1, 3, and 6, the self-powered piezoelectric UV photodetector generated a sufficient output voltage to light up one, three, and six LEDs, respectively, as presented in Fig. 7(c), Fig. S14(b) and Fig. 7(d), which are screenshots from Videos S2, S3 and S4. To develop a UV radiation warning system for individuals engaged in outdoor activities, measurements were performed outdoors at the same location under different weather conditions. In cloudy weather with a UVI of 1, continuous tapping of the self-powered piezoelectric UV photodetector could only light up one LED, as revealed in the photograph and video in Fig. 7(e) and Video S5, respectively. Additionally, in sunny weather with a UVI of 6, six LEDs were lit under the continuous tapping of the self-powered piezoelectric UV photodetector, as depicted in the photograph in Fig. 7(f), which was screenshot from Video S6. Based on the results obtained in this work, it is evident that the UATA-treated TiO_2-NFs:P(VDF-TrFE) self-powered piezoelectric UV photodetector is capable of UVI detection. With the stepping illumination circuit of LEDs, the system can alert individuals engaged in outdoor activities to prevent UV overexposure and skin burning.

4. Conclusion

In summary, TiO_2-NFs:P(VDF-TrFE) nanocomposites were treated by UATA to enhance the β-crystallinity of the films, as confirmed by XRD and FTIR spectra. Under UV irradiation during the UATA, the UV photons absorbed by TiO_2-NFs generated electron-hole pairs via photocatalysis, aligning the polarized dipoles in P(VDF-TrFE) for a superior piezoelectric coefficient. In the FE-SEM images, long and dense needle-shaped crystalline structures were clearly observed in the TiO_2-NFs:P(VDF-TrFE) nanocomposite films. Additionally, the fabricated TiO_2-NFs:P(VDF-TrFE) PENGs supplied a high power density of 3.5×10^{-3} mW/cm^2 with stable operation for at least 600 cycles. Meanwhile, the PENGs could also serve as UV photodetectors to exhibit excellent responsivity and detectivity of 0.14 mA/W and 4×10^8 jones, respectively, under the application of a fixed pressure of 40 kPa at a 2-Hz frequency with UV irradiation. Hence, a UV overexposure warning system was established by connecting a self-powered piezoelectric UV photodetector with a lumped circuit to achieve the stepping illumination of LEDs under continuous tapping, corresponding to UVI levels. Real-time UVI information can remind individuals engaged in outdoor activities to be aware of UV overexposure. Thus, the UATA-treated TiO_2-NFs:P(VDF-TrFE) PENGs possess excellent UV response and self-powered capabilities, which are promising for the future development of UV-assisted portable devices.

CRediT authorship contribution statement

Jer-Chyi Wang: Writing – review & editing, Supervision, Resources, Methodology, Funding acquisition, Conceptualization. **Tzu-Chuan Yang:** Writing – original draft, Validation, Investigation, Data curation. **Tzu-Wei Hsu:** Validation, Investigation. **Ping-Jung Huang:** Investigation. **Peng-Nang Chen:** Investigation. **Chen-Yang Tseng:** Investigation. **Ting-Han Lin:** Investigation. **Jia-Mao Chang:** Investigation. **Chang-Heng Liu:** Conceptualization. **Wen-Ling Yeh:** Conceptualization. **Ming-Chung Wu:** Resources, Methodology.

Declaration of competing interest

The authors declare that they have no known competing financial interests or personal relationships that could have appeared to influence the work reported in this paper.

Acknowledgements

This research was supported by National Science and Technology

Council, R.O.C. (Contract Nos. of NSTC 112–2221-E-182–062-MY3 and NSTC 112–2221-E-182–063-MY2) and Chang Gung Memorial Hospital, Linkou, Taiwan (Contract Nos. of CMRPD2M0101, CMRPD2M0102, CMRPD2M0281, and BMRPA74). The authors would like to thank the Microscopy Center at Chang Gung University for technical assistance.

Supplementary materials

Supplementary material associated with this article can be found, in the online version, at doi:10.1016/j.jtice.2024.105808.

References

[1] Stolarski RS, Douglass AR, Oman LD, Waugh DW. Impact of future nitrous oxide and carbon dioxide emissions on the stratospheric ozone layer. Environ Res Lett 2015;10:034011. https://doi.org/10.1088/1748-9326/10/3/034011.
[2] Barnes PW, Williamson CE, Lucas RM, Robinson SA, Madronich S, Paul ND, Bornman JF, Bais AF, Sulzberger B, Wilson SR, Andrady AL, McKenzie RL, Neale PJ, Austin AT, Bernhard GH, Solomon KR, Neale RE, Young PJ, Norval M, Rhodes LE, Hylander S, Rose KC, Longstreth J, Aucamp PJ, Ballaré CL, Cory RM, Flint SD, de Gruijl FR, Häder DP, Heikkilä AM, Jansen MAK, Pandey KK, Robson TM, Sinclair CA, Wängberg SÅ, Worrest RC, Yazar S, Young AR, Zepp RG. Ozone depletion, ultraviolet radiation, climate change and prospects for a sustainable future. Nat. Sustain 2019;2:569–79. https://doi.org/10.1038/s41893-019-0314-2.
[3] de Gruijl FR, van der Leun JC. Ozone depletion and ultraviolet radiation. CMAJ 2000;163:851–5. https://doi.org/10.23937/2469-5718/1510052.
[4] Faur CI, Moldovan MA, Văleanu M, Rotar H, Filip L, Roman RC. The prevalence and treatment costs of non-melanoma skin cancer in Cluj-Napoca Maxillofacial Center. Medicina (B Aires) 2023;59:1–13. https://doi.org/10.3390/medicina59020220.
[5] World Health Organization. Global solar uv index—a practical guide. Geneva: WHO; 2002.
[6] Sánchez-Pérez JF, Vicente-Agullo D, Barberá M, Castro-Rodríguez E, Cánovas M. Relationship between ultraviolet index (UVI) and first-, second- and third-degree sunburn using the Probit methodology. Sci Rep 2019;9:733–45. https://doi.org/10.1038/s41598-018-36850-x.
[7] McKenzie R, Smale D, Kotkamp M. Relationship between UVB and erythemally weighted radiation. Photochem Photobiol Sci 2004;3:252–6. https://doi.org/10.1039/b312985c.
[8] Sánchez-Pérez JF, Ferradás EG, Alonso FD, García DP, Cano MVM, Cotorruelo JÁB. New Probit equations for the calculation of thermal effects on humans. Process Saf Environ Prot 2010;88:109–13. https://doi.org/10.1016/j.psep.2009.11.007.
[9] Lee J, Kumar N, Patel M, Ghosh S, Kim J. Transparent metal-oxide personal UV monitoring device with machine learning advancement. Sens. Actuators A: Phys. 2023;362:114627. https://doi.org/10.1016/j.sna.2023.114627.
[10] Sun C, Guo H, Yuan L, Tang X, Zhang Y, Song Q, Zhang Y. Analysis of SiC NPN ultraviolet phototransistor under ultrahigh temperature. IEEE Trans Electron Devices 2023;70:2342–6. https://doi.org/10.1109/TED.2023.3255836.
[11] Chekke T, Narzary R, Ngadong S, Satpati B, Bayan S, Das U. Au decorated ultrathin WS_2-based single-electrode triboelectric nanogenerator for flexible self-powered photodetector. Sens. Actuators B Chem. 2023;349:114076. https://doi.org/10.1016/j.sna.2022.114076.
[12] Kumar N, Patel M, Kim J, Jeong C, Wong CP. Flexible transparent photovoltaics for ultra-UV photodetection and functional UV-shielding based on Ga_2O_3/Cu_2O heterojunction. Appl Mater Today 2022;29:101620. https://doi.org/10.1016/j.apmt.2022.101620.
[13] Ye Q, Zhang X, Yao R, Luo D, Liu X, Zou W, Guo C, Xu Z, Ning H, Peng J. Research and progress of transparent, flexible tin oxide ultraviolet photodetector. cryst 2021;11:1479. https://doi.org/10.3390/cryst11121479.
[14] Peng Y, Lu J, Wang X, Ma W, Que M, Chen Q, Li F, Liu X, Gao W, Pan C. Self-powered high-performance flexible GaN/ZnO heterostructure UV photodetectors with piezo-phototronic effect enhanced photoresponse. Nano Energy 2022;94:106945. https://doi.org/10.1016/j.nanoen.2022.106945.
[15] Bakhtar LJ, Abdoos H, Rashidi S. A review on fabrication and in vivo applications of piezoelectric nanocomposites for energy harvesting. J Taiwan Inst Chem Eng 2023;148:104651. https://doi.org/10.1016/j.jtice.2022.104651.
[16] Raj NPMJ, Alluri NR, Khandelwal G, Kim SJ. Lead-free piezoelectric nanogenerator using lightweight composite films for harnessing biomechanical energy. Compos. B Eng. 2019;161:608–16. https://doi.org/10.1016/j.compositesb.2018.12.129.
[17] Qin W, Zhou P, Xu X, Huang C, Srinivasan G, Qi Y, Zhang T. High-performance piezoelectric nanogenerator based on low-entropy structured nanofibers for a multi-mode energy harvesting and self-powered ultraviolet photodetector. ACS Appl. Electron. Mater. 2020;4:2970–8. https://doi.org/10.1021/acsaelm.2c00411.
[18] Zheng X, Liu Z, Wang R, Chen A. Bending-insensitive intrinsically flexible ultraviolet encoding devices based on piezoelectric nanogenerator- Supplied liquid crystalline polymer fabrics. Small 2022;18:2202639. https://doi.org/10.1002/smll.202202639.
[19] Pi Z, Zhang J, Wen C, Zhang Z, Wu D. Flexible piezoelectric nanogenerator made of poly(vinylidenefluoride-co-trifluoroethylene) (PVDF-TrFE) thin film. Nano Energy 2014;7:33–41. https://doi.org/10.1016/j.nanoen.2014.04.016.
[20] Mohammadpourfazeli S, Arash S, Ansari A, Yang S, Mallick K, Bagherzadeh R. Future prospects and recent developments of polyvinylidene fluoride (PVDF) piezoelectric polymer; fabrication methods, structure, and electro-mechanical properties. RSC Adv 2023;13:370–87. https://doi.org/10.1039/D2RA06774A.
[21] Wang JC, Jiang YP, Lin YJ, Chan SH, Wu MC. Trifluoroethylene bond enrichment in P(VDF-TrFE) copolymers with enhanced ferroelectric behaviors by plasma fluorination on bottom electrode. J Taiwan Inst Chem Eng 2020;107:152–60. https://doi.org/10.1016/j.jtice.2019.11.005.
[22] Tanaka H, Lovinger AJ, Davis DD. Miscibility and isomorphic cocrystallization in blends of ferroelectric copolymers of vinylidene fluoride and trifluoroethylene. J Polym Sci B: Polym Phys 1990;28:2183–98. https://doi.org/10.1002/polb.1990.090281202.
[23] Turdakyn N, Bekezhankyzy Z, Araby S, Montazami R, Bakenov Z, Kalimuldina G. Investigation of electrospun piezoelectric P(VDF-TrFE) nanofiber-based nanogenerators for energy harvesting. Energy Rep 2023;10:628–36. https://doi.org/10.1016/j.egyr.2023.07.010.
[24] Yang TC, Jiang YP, Lin TH, Chen SH, Ho CM, Wu MC, Wang JC. N-butylamine-modified graphite nanoflakes blended in ferroelectric P(VDF-TrFE) copolymers for piezoelectric nanogenerators with high power generation efficiency. Eur Polym J 2021;159:110754. https://doi.org/10.1016/j.eurpolymj.2021.110754.
[25] Sultana A, Sadhukhan P, Alam MM, Das S, Middya TR, Mandal D. Organo-lead halide perovskite induced electroactive β-phase in porous PVDF films: an excellent material for photoactive piezoelectric energy harvester and photodetector. ACS Appl Mater Interfaces 2018;10:4121–30. https://doi.org/10.1021/acsami.7b17408.
[26] Patel M, Park HH, Bhatnagar P, Kumar N, Lee J, Kim J. Transparent integrated pyroelectric-photovoltaic structure for photo-thermo hybrid power generation. Nat Commun 2024;15:3466. https://doi.org/10.1038/s41467-024-47483-2.
[27] Nguyen TT, Kumar N, Lee J, Patel M, Kim J. All-transparent tandem photovoltaic-powered photodetector. Nano Energy 2023;116:108815. https://doi.org/10.1016/j.nanoen.2023.108815.
[28] Yang H. An introduction to ultraviolet detectors based on III group-nitride semiconductor. J. Phys.: Conf. Ser. 2020;1676:012072. https://doi.org/10.1088/1742-6596/1676/1/012072.
[29] Huang TY, Chen CH, Lin CC, Lee YJ, Liu CL, Liou GS. UV-sensing organic phototransistor memory devices with a doped organic polymer electret composed of triphenylamine-based aggregation-induced emission luminogens. J Mater Chem C 2019;7:11014–21. https://doi.org/10.1039/c9tc03607e.
[30] Kaur D, Pal B. Improved photocatalytic activity of graphene oxide modified Ag-TiO_2 for degradation of piroxicam-20 and dehydrogenation of methanol under light irradiation. J Taiwan Inst Chem Eng 2024;155:105282. https://doi.org/10.1016/j.jtice.2023.105282.
[31] Winayu BNR, Chou CC, Chu H. Enhancement of toluene photocatalytic degradation using GO/S/TiO_2,". J Taiwan Inst Chem Eng 2022;139:104529. https://doi.org/10.1016/j.jtice.2022.104529.
[32] Hanaor DAH, Sorrell CC. Review of the anatase to rutile phase transformation. J Mater Sci 2011;46:855–74. https://doi.org/10.1007/s10853-010-5113-0.
[33] Chen X, Hosseini SN, van Huis MA. Heating-induced transformation of anatase TiO_2 nanorods into rock-salt TiO nanoparticles: implications for photocatalytic and gas-sensing applications. ACS Appl Nano Mater 2022;5:1600–6. https://doi.org/10.1021/acsanm.1c04346.
[34] Martín-Gonzalez MA, Fernandez-Rodríguez C, Gonzalez-Díaz OM, Susial P, Dona-Rodríguez JM. Open-cell ceramic foams covered with TiO_2 for the photocatalytic treatment of agro-industrial wastewaters containing imazalil at semi-pilot scale. J Taiwan Inst Chem Eng 2023;147:104902. https://doi.org/10.1016/j.jtice.2023.104902.
[35] Nie X, Zhuo S, Maeng G, Sohlberg K. Doping of TiO_2 polymorphs for altered optical and photocatalytic properties. Int J Photoenergy 2009;2009:294042. https://doi.org/10.1155/2009/294042.
[36] Withers AC, Essene EJ, Zhang Y. Rutile/TiO_2II phase equilibria. Contrib Mineral Petrol 2003;145:199–204. https://doi.org/10.1007/s00410-003-0445-2.
[37] Swamy V, Gale JD, Dubrovinsky LS. Atomistic simulation of the crystal structures and bulk moduli of TiO_2 polymorphs. J Phys Chem Solids 2001;62:887–95. https://doi.org/10.1016/S0022-3697(00)00246-8.
[38] Ren R, Yang Z, Shaw LL. Polymorphic transformation and powder characteristics of TiO_2 during high energy milling. J Mater Sci 2000;35:6015–26. https://doi.org/10.1023/A:1026751017284.
[39] Lin TH, Wu MC, Chiang KP, Chang YH, Hsu JF, Hsu KH, Lee KM. Unveiling the surface precipitation effect of Ag ions in Ag-doped TiO_2 nanofibers synthesized by one-step hydrothermal method for photocatalytic hydrogen production. J Taiwan Inst Chem Eng 2021;120:291–9. https://doi.org/10.1016/j.jtice.2021.03.011.
[40] Ismailov SM, Omarov ZM, Velikhanov AR. Effect of plastic deformation on the specific heat of silicon. High Temp 2019;57:124–6. https://doi.org/10.1134/S0018151X19010139.
[41] Xia W, Wang Z, Xing J, Cao Congjun, Xu Zhuo. The dependence of dielectric and ferroelectric properties on crystal phase structures of the hydrogenized P(VDF-TrFE) films with different thermal processing. IEEE Trans Ultrason Ferroelectr Freq Control 2016;63:1674–80. https://doi.org/10.1109/TUFFC.2016.2594140.
[42] Shepelin NA, Lussini VC, Fox PJ, Dicinoski GW, Glushenkov AM, Shapter JG, Ellis AV. 3D printing of poly(vinylidene fluoride-trifluoroethylene): a poling-free technique to manufacture flexible and transparent piezoelectric generators. MRS Commun 2019;9:159–64. https://doi.org/10.1557/mrc.2019.19.
[43] Roy K, Ghosh SK, Sultana A, Garain S, Xie M, Bowen CR, Henkel K, Schmeißer D, Mandal D. A self-powered wearable pressure sensor and pyroelectric breathing sensor based on GO interfaced PVDF nanofibers. ACS Appl Nano Mater. 2019;2:2013–25. https://doi.org/10.1021/acsanm.9b00033.

[44] Higazy AA, Issa MR, Kassem ME. Optical studies in polyvinylidene difluoride material (PVDF). Radiat Eff. Defect Solid: Incorp Plasma Sci and Plasma Tech. 1994;129:293–9. https://doi.org/10.1080/10420159408229029.
[45] Zillohu AU, Alissawi N, Abdelaziz R, Elbahri M. Thermo-plasmonics for localized graphitization and welding of polymeric nanofibers. Materials (Basel) 2014;7:323–32. https://doi.org/10.3390/ma7010323.
[46] Meng N, Zhu X, Mao R, Reece MJ, Bilotti E. Nanoscale interfacial electroactivity in PVDF/PVDF-TrFE blended films with enhanced dielectric and ferroelectric properties. J Mater Chem C 2017;5:3296–305. https://doi.org/10.1039/c7tc00162b.
[47] Xu F, Zhang K, Zhou Y, Qu Z, Wang H, Zhang Y, Zhou H, Yan C. Facile preparation of highly oriented poly(vinylidene fluoride) uniform films and their ferro- and piezoelectric properties. RSC Adv 2017;7:17038. https://doi.org/10.1039/c7ra00586e.
[48] Atif R, Khaliq J, Combrinck M, Hassanin AH, Shehata N, Elnabawy E, Shyha I. Solution blow spinning of polyvinylidene fluoride based fibers for energy harvesting applications: a review. Polymers (Basel) 2020;12:1304. https://doi.org/10.3390/polym12061304.
[49] Zaszczyńska A, Sajkiewicz PŁ, Gradys A, Tymkiewicz R, Urbanek O, Kołbuk D. Influence of process-material conditions on the structure and biological properties of electrospun polyvinylidene fluoride fibers. Bull Pol Ac: Tech. 2020;68:627–33. https://doi.org/10.24425/bpasts.2020.133368.
[50] Cai X, Lei T, Sun D, Lin L. A critical analysis of the a, b and g phases in poly (vinylidene fluoride) using FTIR. RSC Adv 2017;7:15382. https://doi.org/10.1039/c7ra01267e.
[51] Lu T, Solis-Ramos E, Yi Y, Kumosa M. UV degradation model for polymers and polymer matrix composites. Polym Degrad Stab 2018;154:203–10. https://doi.org/10.1016/j.polymdegradstab.2018.06.004.
[52] Feng T, Xie D, Zang Y, Wu X, Ren T, Pan W. Temperature control of P(VDF-TrFE) copolymer thin films. Integr Ferroelectr 2013;141:187–94. https://doi.org/10.1080/10584587.2012.694748.
[53] Bhadwal N, Mrad RB, Behdinan K. Review of piezoelectric properties and power output of PVDF and copolymer-based piezoelectric nanogenerators. Nanomaterials 2023;13:3170. https://doi.org/10.3390/nano13243170.
[54] Guo HF, Li ZS, Dong SW, Chen WJ, Deng L, Wang YF, Ying DJ. Piezoelectric PU/PVDF electrospun scaffolds for wound healing applications. Colloids Surf B: Biointerfaces 2013;96:29–36. https://doi.org/10.1016/j.colsurfb.2012.03.014.
[55] Ejehi F, Shooshtari L, Mohammadpour R, Asadian E, Sasanpour P. Self-powered ultraviolet/visible photodetector based on graphene-oxide via triboelectric nanogenerators performing by finger tapping. Nanotechnol 2022;33:475205. https://doi.org/10.1088/1361-6528/ac8a52.
[56] Chen Y, Su L, Jiang M, Fang X. Switch type PANI/ZnO core-shell microwire heterojunction for UV photodetection. J Mater Sci 2022;105:259–65. https://doi.org/10.1016/j.jmst.2021.07.031.
[57] Seliverstova EV, Ibrayev NK, Zhumabekov AZ. The effect of silver nanoparticles on the photodetecting properties of the TiO_2/graphene oxide nanocomposite. Opt Spectrosc 2020;128:1449–57. https://doi.org/10.1134/S0030400X20090192.
[58] Khan MA, Kumar A, Zhang J, Kumar M. Recent advances and prospects in reduced graphene oxide-based photodetectors. J Mater Chem C 2021;9:8129–57. https://doi.org/10.1039/D1TC01306H.
[59] Sengupta P, Sadhukhan P, Saha S, Das S, Ray R. Improved energy harvesting ability of $C_3H_7NH_3PbI_3$ decorated PVDF nanofiber based flexible nanogenerator. Nano Energy 2023;109:108277. https://doi.org/10.1016/j.nanoen.2023.108277.
[60] Kadir ES, Gayen RN, Chowdhury MP. Enhanced photodetection properties of GO incorporated flexible PVDF membranes under solar spectrum. J Polym Res 2022;29:529. https://doi.org/10.1007/s10965-022-03364-0.
[61] Bayan S, Bhattacharya D, Mitra RK, Ray SK. Self-powered flexible photodetectors based on Ag nanoparticle-loaded g-C_3N_4 nanosheets and PVDF hybrids: role of plasmonic and piezoelectric effects. Nanotechnol 2020;31:365401. https://doi.org/10.1088/1361-6528/ab9470.